



The Impact of Back-Sputtered Carbon on the Accelerator Grid Wear Rates of the NEXT and NSTAR Ion Thrusters

George C. Soulas
Glenn Research Center, Cleveland, Ohio

NASA STI Program . . . in Profile

Since its founding, NASA has been dedicated to the advancement of aeronautics and space science. The NASA Scientific and Technical Information (STI) program plays a key part in helping NASA maintain this important role.

The NASA STI Program operates under the auspices of the Agency Chief Information Officer. It collects, organizes, provides for archiving, and disseminates NASA's STI. The NASA STI program provides access to the NASA Aeronautics and Space Database and its public interface, the NASA Technical Reports Server, thus providing one of the largest collections of aeronautical and space science STI in the world. Results are published in both non-NASA channels and by NASA in the NASA STI Report Series, which includes the following report types:

- **TECHNICAL PUBLICATION.** Reports of completed research or a major significant phase of research that present the results of NASA programs and include extensive data or theoretical analysis. Includes compilations of significant scientific and technical data and information deemed to be of continuing reference value. NASA counterpart of peer-reviewed formal professional papers but has less stringent limitations on manuscript length and extent of graphic presentations.
- **TECHNICAL MEMORANDUM.** Scientific and technical findings that are preliminary or of specialized interest, e.g., quick release reports, working papers, and bibliographies that contain minimal annotation. Does not contain extensive analysis.
- **CONTRACTOR REPORT.** Scientific and technical findings by NASA-sponsored contractors and grantees.

- **CONFERENCE PUBLICATION.** Collected papers from scientific and technical conferences, symposia, seminars, or other meetings sponsored or cosponsored by NASA.
- **SPECIAL PUBLICATION.** Scientific, technical, or historical information from NASA programs, projects, and missions, often concerned with subjects having substantial public interest.
- **TECHNICAL TRANSLATION.** English-language translations of foreign scientific and technical material pertinent to NASA's mission.

Specialized services also include creating custom thesauri, building customized databases, organizing and publishing research results.

For more information about the NASA STI program, see the following:

- Access the NASA STI program home page at <http://www.sti.nasa.gov>
- E-mail your question to help@sti.nasa.gov
- Fax your question to the NASA STI Information Desk at 443-757-5803
- Phone the NASA STI Information Desk at 443-757-5802
- Write to:
STI Information Desk
NASA Center for AeroSpace Information
7115 Standard Drive
Hanover, MD 21076-1320



The Impact of Back-Sputtered Carbon on the Accelerator Grid Wear Rates of the NEXT and NSTAR Ion Thrusters

George C. Soulas
Glenn Research Center, Cleveland, Ohio

Prepared for the
33rd International Electric Propulsion Conference (IEPC2013)
sponsored by the Electric Rocket Propulsion Society
Washington, D.C., October 6–10, 2013

National Aeronautics and
Space Administration

Glenn Research Center
Cleveland, Ohio 44135

Acknowledgments

The author thanks Dr. James E. Polk for his invaluable help, comments, and suggestions. This work was funded by the NASA Science Mission Directorate's In Space Propulsion Technology Program Office at the NASA Glenn Research Center.

This report contains preliminary findings,
subject to revision as analysis proceeds.

Level of Review: This material has been technically reviewed by technical management.

Available from

NASA Center for Aerospace Information
7115 Standard Drive
Hanover, MD 21076-1320

National Technical Information Service
5301 Shawnee Road
Alexandria, VA 22312

Available electronically at <http://www.sti.nasa.gov>

The Impact of Back-Sputtered Carbon on the Accelerator Grid Wear Rates of the NEXT and NSTAR Ion Thrusters

George C. Soulas
National Aeronautics and Space Administration
Glenn Research Center
Cleveland, Ohio 44135

Abstract

A study was conducted to quantify the impact of back-sputtered carbon on the downstream accelerator grid erosion rates of the NASA's Evolutionary Xenon Thruster (NEXT) Long Duration Test. A similar analysis that was conducted for the NASA's Solar Electric Propulsion Technology Applications Readiness Program (NSTAR) Life Demonstration Test was used as a foundation for the analysis developed herein. A new carbon surface coverage model was developed that accounted for multiple carbon adlayers before complete surface coverage is achieved. The resulting model requires knowledge of more model inputs, so they were conservatively estimated using the results of past thin film sputtering studies and particle reflection predictions. In addition, accelerator current densities across the grid were rigorously determined using an ion optics code to determine accelerator current distributions and an algorithm to determine beam current densities along a grid using downstream measurements. The improved analysis was applied to the NSTAR test results for evaluation. The improved analysis demonstrated that the impact of back-sputtered carbon on pit and groove wear rate for the NSTAR LDT was negligible throughout most of eroded grid radius. The improved analysis also predicted the accelerator current density for transition from net erosion to net deposition considerably more accurately than the original analysis. The improved analysis was used to estimate the impact of back-sputtered carbon on the accelerator grid pit and groove wear rate of the NEXT Long Duration Test. Unlike the NSTAR analysis, the NEXT analysis was more challenging because the thruster was operated for extended durations at various operating conditions and was unavailable for measurements because the test is ongoing. As a result, the NEXT LDT estimates presented herein are considered preliminary until the results of future post-test analyses are incorporated. The worst-case impact of carbon back-sputtering was determined to be the full power operating condition, but the maximum impact of back-sputtered carbon was only a 4 percent reduction in wear rate. As a result, back-sputtered carbon is estimated to have an insignificant impact on the first failure mode of the NEXT LDT at all operating conditions.

Nomenclature

dA_{erode}/dA_o	Ratio of pit and groove eroded area to the hexagon area surrounding a single aperture
$(dE/dx)_e$	Electronic stopping power
$(dE/dx)_n$	Nuclear stopping power
e	Electron charge
i	Adsorbate adlayer ($i = 0$ denotes the substrate surface)
j_a	Average accelerator current density in the pit and groove erosion pattern
J_a	Accelerator current
$j_{a-trans}$	Average accelerator current density at transition from net erosion to net deposition
J_{aw}	Accelerator current collected by the accelerator aperture barrel walls
j_b	Beam current density along the accelerator grid
J_b	Beam current

N_c	Surface density of substrate adsorption sites occupied by adatoms
NEXT	NASA's Evolutionary Xenon Thruster
NEXT LDT	NEXT Long Duration Test
N_o	Surface density of substrate adsorption sites
NSTAR	NASA's Solar Electric Propulsion Technology Applications Readiness Program
NSTAR LDT	NSTAR Life Demonstration Test
R_i	Particle projectile range
R_N	Particle reflection coefficient (the ratio of reflected-to-total particles incident on a surface)
s	Adsorbate sticking coefficient
V_a	Accelerator power supply output voltage
V_{beam}	Beam plasma potential
V_{cex}	Charge exchange ion energy
V_g	Coupling voltage
Y	Sputter yield
γ_C	Carbon back-sputter flux
θ_i	Fractional surface coverage of adlayer i
θ_c	Total fractional surface coverage of substrate adsorption sites by adsorbate

Subscripts and Superscripts:

C	Carbon adsorbate
$C-Mo$	Single carbon adsorbate adlayer on a molybdenum substrate
i	Adsorbate adlayer ($i = 0$ denotes the substrate surface)
max	Maximum value
Mo	Molybdenum substrate
net	Net value
trans	Transition from net erosion to net deposition

I. Introduction

The NASA Glenn Research Center is responsible for the development of NASA's Evolutionary Xenon Thruster (NEXT) ion propulsion system (Ref. 1). The NEXT system is a next generation ion propulsion system to follow the successful NASA's Solar Electric Propulsion Technology Applications Readiness Program (NSTAR) ion propulsion system that propelled NASA's Deep Space 1 spacecraft and is presently propelling the Dawn spacecraft (Refs. 2 and 3). The objective of the NEXT project is to advance this propulsion technology to NASA Technology Readiness Level 5, with significant progress towards level 6, to support NASA Science Mission Directorate missions (Ref. 4). Propulsion system elements under development by the NEXT program include a high performance, 7 kW ion thruster; a modular, high-efficiency 7 kW power processor unit; a highly flexible advanced xenon propellant management system; and a compact, light-weight thruster gimbal. This design approach was selected to provide future NASA science missions with the greatest value in mission performance benefit at a low total development cost (Ref. 1).

The service life capabilities of NEXT and NSTAR ion thrusters were assessed via analyses (e.g., see Refs. 5 and 6) and long duration tests (e.g., see Refs. 7 to 11). During the operation of any long duration test, accelerator grid wear rates are affected by two competing, facility-induced effects. The facility

background pressures are higher than that in space due to pumping speed limitations. This leads to a higher neutral density near the accelerator grid and therefore the creation of more charge-exchange ions at the accelerator grid region, which subsequently enhances accelerator grid wear rates. However, energetic ions from the thruster's exhaust plume will also sputter-erode downstream vacuum facility surfaces. This sputter-eroded facility material is ejected in all directions, including upstream towards the ion thruster and its exposed accelerator grid. The phenomenon of depositing this sputter-eroded vacuum facility material back onto a thruster is commonly referred to as back-sputtering. The back-sputtering of eroded facility material onto the thruster's accelerator downstream grid can potentially introduce an unwanted effect where the accelerator grid downstream surface erosion rate is masked by the arrival rate of back-sputtered facility material. To mitigate this effect, sputter-eroded facility walls are lined with a low sputter yield material, typically carbon in the form of graphite. Unfortunately, there is a concern that carbon deposition on critical accelerator grid erosion sites can significantly reduce their erosion rates compared to that in space (Ref. 12).

The NEXT ion thruster service life capability is being assessed, in part, via a long duration test (NEXT LDT) that was initiated in June 2005 and is still operational today (Ref. 7). The objectives of this test are to demonstrate the initial project qualification propellant throughput requirement of 450 kg, validate thruster service life modeling predictions, quantify thruster performance and erosion as a function of engine wear and throttle level, and identify unknown life-limiting mechanisms. After demonstration of the qualification propellant throughput of 450 kg of xenon, the first objective was redefined to test to failure or as long as project funding permits. In September of 2013, the thruster exceeded 50,000 h of accumulated operation and 900 kg of propellant throughput with a demonstrated total impulse of > 34.8 MN·s over a range of power-throttled operating conditions. The NEXT LDT has set electric propulsion records for the most hours of operation, highest propellant throughput processed, greatest total impulse demonstrated, and longest hollow cathode operation (Ref. 7).

A detailed service life assessment was also conducted in parallel with the NEXT LDT (Ref. 5). All credible thruster failure modes were assessed over the full power throttling range of the NEXT ion thruster. The first failure mode of the NEXT thruster over the entire power throttling range was predicted to be structural failure of the accelerator grid. This failure mode is due to sputter erosion of the downstream accelerator grid surface by charge-exchange ions created in this region. These eroding ions create a hexagonal "pit and groove" erosion pattern that surrounds each aperture as shown in Figure 1. Because the NEXT LDT ion thruster is operated in a vacuum facility that is lined with graphite panels (Ref. 7), this thruster wear is subject to carbon back-sputtering. As a result, the impact of back-sputtered carbon on accelerator grid pit and groove wear rate must be assessed to verify that the objectives of the test are being met.

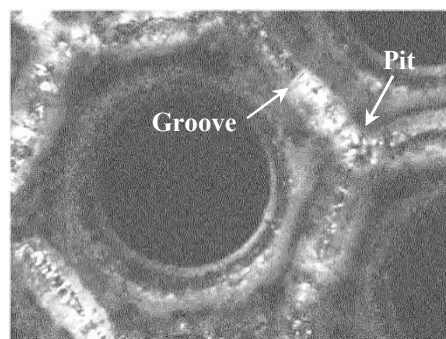


Figure 1.—The NEXT LDT accelerator grid center aperture at 19,520 h showing the pit and groove erosion pattern. Darker regions are net carbon deposition while lighter regions are net molybdenum erosion.

Following the NSTAR Life Demonstration Test (NSTAR LDT), a detailed analysis was conducted to assess the effects of carbon deposition on accelerator grid pit and groove wear rate (Refs. 11 and 12). A surface coverage time rate of change model was developed to assess the impact of back-sputtered carbon on the sputter yield of the molybdenum accelerator grid surface. Sputter yields of a single carbon monolayer adsorbed onto a molybdenum surface were both measured and determined theoretically based on a model by Sigmund and Winters (Ref. 13). Both measured and theoretically-determined sputter yields for a single carbon monolayer were found to be much higher than that of bulk carbon. Unfortunately, the surface coverage model was unable to correctly predict the measured location of the transition from net grid erosion to net carbon deposition using these higher yields. This ultimately brought into question the efficacy of the analysis.

The objective of this paper is to quantify the impact of back-sputtered carbon on the downstream accelerator grid erosion rates for the NEXT LDT. The NSTAR analysis of Reference 12 provides an excellent foundation for the analysis of the NEXT LDT. However, the NSTAR analysis must first be improved to more accurately predict this transition from net erosion to net deposition. This paper is therefore divided into four sections. The analysis for this study is first presented. It includes a description of the original NSTAR analysis with improvements developed for this study. Afterwards, these analysis improvements are evaluated and sensitivities to the model inputs are determined using the NSTAR LDT results. The improved analysis is then applied to the NEXT LDT to determine the impact of back-sputtered carbon on the accelerator grid pit and groove wear rates. Finally, conclusions from this study are presented.

II. Analysis Approach

The NSTAR analysis approach and improvements for this study are described in the following sections. The general model for determining the impact of back-sputtered carbon on accelerator grid wear is initially described. A more rigorous carbon surface coverage model is then presented, which is the primary input to the aforementioned general model. Finally, the various model inputs for this study are determined.

A. Impact of Back-Sputtered Carbon on Accelerator Grid Wear

The following general model for the impact of back-sputtered carbon on accelerator grid pit and groove wear rate is the same as that developed for the NSTAR LDT analysis in Reference 12 and is presented here for completeness. There are three particles involved in the sputter erosion process at the accelerator grid surface in the presence of carbon back-sputtering: the xenon ion, the molybdenum grid substrate, and the carbon adsorbate. Molybdenum has a body-center cubic lattice with a total carbon adsorption site surface density, N_o , of $1.0 \times 10^{15} \text{ cm}^{-2}$. If N_c is the number density of adsorbed carbon atoms (or adatoms) occupying those potential adsorption sites, then the fractional substrate surface coverage by adsorbate adatoms, θ_c , is given by:

$$\theta_c = \frac{N_c}{N_o}. \quad (1)$$

The fractional surface coverage will later be shown to be a function of parameters that can vary across a grid (e.g., accelerator current density), so θ_c represents the fractional surface coverage of a differential area along the grid.

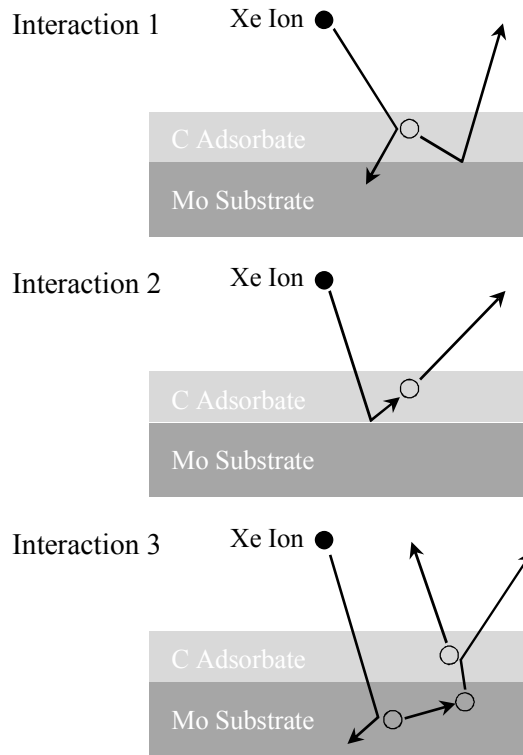


Figure 2.—Collisional interactions between ion, adsorbate, and substrate atoms.

For the moment, adsorbed carbon is assumed to form no more than a single monolayer on the molybdenum substrate and that the fractional substrate surface coverage is small (i.e., $\theta_c \ll 1$). According to Sigmund and Winters, there are three potential interactions that can occur when a xenon ion bombards the surface of the molybdenum accelerator grid and these are depicted in Figure 2 (Ref. 13). For the first interaction, the xenon ion collides with a carbon adatom, elastically transferring a portion of its kinetic energy to the adatom, which subsequently reflects from the substrate surface. For the second interaction, the xenon ion reflects from the molybdenum substrate and collides with a carbon adatom. For the third interaction, the xenon ion collides with the molybdenum substrate, initiating a collisional cascade that causes a molybdenum substrate atom(s) to collide with a carbon adatom, transferring a portion of its kinetic energy to the adatom. For all three interactions, the adatom escapes the surface only if its energy normal to the surface is greater than the adsorbate surface binding energy. Finally, there is an increased probability that a single xenon ion can cause more than one interaction as the fractional substrate surface coverage approaches complete coverage (i.e., $\theta_c \rightarrow 1$).

The ion and substrate atoms colliding with adsorbate adatoms for the first and third interactions only transfer a portion of their kinetic energy, so some substrate sputtering still occurs even in the presence of single carbon monolayer surface coverage. However, substrate sputtering can be eliminated in the presence multiple carbon adsorbed monolayers, or adlayers. Multiple adlayers of carbon adsorbate result in xenon ion energy dissipation as it penetrates the adsorbate surface. If the number of adlayers is large enough, no substrate sputtering occurs. Because multiple adlayers of carbon adsorbate will be shown to exist for $\theta_c < 1$, it can be assumed that the net sputter yield of the molybdenum substrate, Y_{Mo}^{net} , is given by (Ref. 12):

$$Y_{Mo}^{net} = Y_{Mo} \cdot (1 - \theta_c). \quad (2)$$

Here, Y_{Mo} is the sputter yield of the bulk molybdenum substrate. The above equation conservatively assumes that any carbon surface coverage results in the elimination of molybdenum substrate sputtering at that site. This equation defines an average sputter yield of a molybdenum substrate covered with carbon adatoms, and therefore represents a macroscopic quantity. Rearranging this equation yields:

$$\frac{Y_{Mo}^{net}}{Y_{Mo}} = 1 - \theta_c . \quad (3)$$

The above ratio represents a correction factor for the accelerator grid wear rate in the presence of carbon back-sputtering. Because $0 < \theta_c \leq 1$ in the presence of back-sputtering, back-sputtered carbon acts to reduce the accelerator grid wear rate demonstrated in ground test facilities. And because this net to bulk molybdenum sputter yield ratio is a function of θ_c , this ratio can vary along the surface of the grid. All that remains is to determine θ_c , which is the topic of the next section.

B. Carbon Surface Coverage Model

Development of a carbon surface coverage model requires an understanding of the thin film growth processes. During a sputter deposition process, sputtered adsorbate collides with the substrate surface atoms. If the subsequent elastic collisions are sufficient to dissipate the adsorbate kinetic energy normal to the surface, the adsorbate can be physisorbed onto the substrate surface to create an adatom. While physisorbed on the surface, these adatoms can diffuse along the surface to form and grow clusters. Clusters can also form and grow due to direct adatom collision. After reaching a certain critical size, the clusters become stable nuclei and are chemisorbed onto the surface, marking the start of the nucleation stage. During this stage, these nuclei grow in number and size until a saturation nucleation density is achieved. During this growth process, the nuclei exhibit one of three growth modes (Refs. 14 and 15):

1. Island-type growth (or Volmer-Weber growth), where the nucleus grows both normal and parallel to the substrate surface;
2. Layer-type growth (or Frank van der Merwe growth), where the nucleus grows parallel to the substrate surface layer by layer; and
3. Mixed-type growth (or Stranski-Krastanov growth), where the nucleus typically exhibits a layered-type growth, followed by island-type growth.

The nuclei will eventually coalesce, forming bigger islands in a process called agglomeration. These larger islands eventually merge leaving channels and holes of uncovered substrate surface, which are eventually filled by secondary nucleation and growth (Ref. 14).

In most practical sputter deposition applications, island-type growth occurs (Ref. 14). Layer-type growth requires a lower binding energy between carbon adatoms than that between carbon adatoms and the molybdenum substrate (Ref. 15). Because the primary desorption mechanism in this study is sputtering, this layer-type growth requires the sputter yield of a single carbon monolayer on a molybdenum substrate to be less than that of bulk carbon, a condition that was shown to be violated in Reference 12. As a result, layer- and mixed-type growths are not occurring during back-sputtered carbon adsorption on the accelerator grid.

Another growth mode type can also occur and is called columnar growth. This surface layer growth mode is characterized by ballistic aggregation of adsorbate due to very low adatom surface mobility (Ref. 15). The resulting columnar-like film structure is quite porous and exhibits poor mechanical properties.

Whether island-type or columnar growth is occurring during back-sputtered carbon adsorption on the molybdenum accelerator grid, both growth modes have a common attribute: there are multiple adlayers before complete surface coverage is achieved. As a result, the carbon surface coverage model must account for these multiple carbon adlayers.

For the original NSTAR analysis, the surface coverage time rate of change was described with the model below:

$$N_o \cdot \frac{d\theta_c}{dt} = \gamma_C - \frac{j_a}{e} \cdot Y_{C-Mo} \cdot \theta_c \quad (4)$$

Here, γ_C is the back-sputter flux of carbon adsorbate, j_a is the accelerator ion current density in the pit and groove erosion pattern, e is the electron charge, and Y_{C-Mo} is the sputter yield of a single carbon adlayer on a molybdenum substrate. To determine equilibrium surface coverage, $d\theta_c/dt$ is set equal to zero and the result is solved for θ_c :

$$\theta_c = \frac{e \cdot \gamma_c}{j_a \cdot Y_{C-Mo}} \quad (5)$$

However, this equation lacks adequate rigor because it fails to account for the growth of multiple carbon adlayers before complete surface coverage is achieved. In addition, it fails to distinguish between adsorption onto substrate versus existing adsorbate surface coverage.

So, for this study, a more rigorous carbon surface coverage model was developed. The basis for this is a model developed by Brunauer, Emmitt, and Teller that was originally used to describe the physisorption of additional gas adlayers on a chemisorbed adlayer (Ref. 16). For the development of this model, the following assumptions were made:

1. Back-sputtered carbon adsorbate can be adsorbed both onto a molybdenum substrate and existing carbon adatoms, allowing for a range of adlayers before complete surface coverage is achieved.
2. Carbon adatom surface diffusion is neglected. Although some surface diffusion is likely occurring, surface diffusion is likely limited by ion bombardment. The evidence for this is shown in Figure 3 for the NSTAR LDT accelerator grid surface at the transition from net erosion to net deposition. The image shows carbon deposition throughout most of the surface. However, the carbon film in the pit and groove erosion pattern is significantly porous compared to the films next to it. And the only difference between these sites is the degree of ion bombardment. Significant ion bombardment is speculated to have caused sputter-induced desorption of the weakly-bonded physisorbed carbon, limiting its mobility on the film and substrate surfaces.
3. Carbon adsorbate bulk diffusion is neglected. Thermally-induced bulk diffusion is limited by the low anticipated molybdenum substrate temperature (i.e., an anticipated grid temperature of approximately 200 °C versus the 3650 °C sublimation temperature for graphite) (Ref. 17). However there can be sputter-induced redistribution of adsorbate particles, which is neglected here.
4. Carbon adatoms only stack one on top of another, so N_o is constant for all adlayers. Graphite, which has a stacked hexagonal lattice, has surface densities of $3.8 \times 10^{15} \text{ cm}^{-2}$ along the hexagonal plane and $1.4 \times 10^{15} \text{ cm}^{-2}$ perpendicular to it. Although this varying N_o is not captured by the model, the carbon film in the pit and groove pattern was shown to be porous with a density ≤ 60 percent of maximum theoretical density of graphite (Ref. 12).
5. The only carbon desorption mechanism is sputter erosion. Ho et al. showed that thermal desorption for a single carbon adlayer on a molybdenum substrate is negligible for temperatures $< 300 \text{ °C}$ (Ref. 18). And sublimation of bulk carbon in the form of graphite requires significantly higher temperatures.
6. Sputter erosion can only remove a surface carbon adatom and not underlying atoms.
7. Carbon adsorption onto either the molybdenum substrate or carbon adsorbate includes a sticking coefficient.

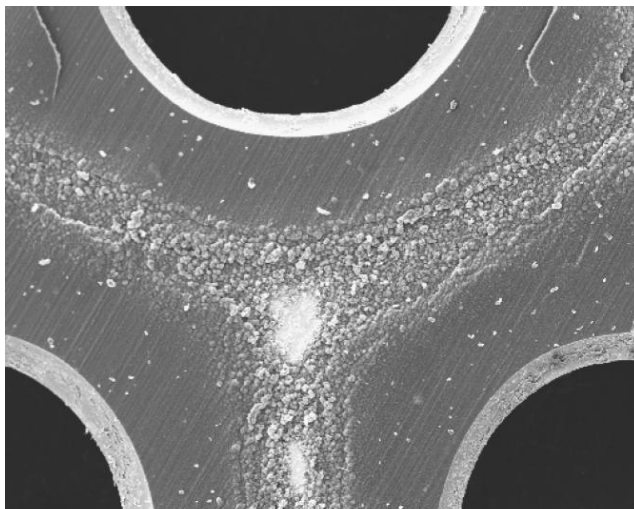


Figure 3.—Scanning electron photomicrograph of the downstream NSTAR accelerator grid at 11.8 cm from the center of the grid (Ref. 12). White areas are molybdenum and gray areas are carbon.

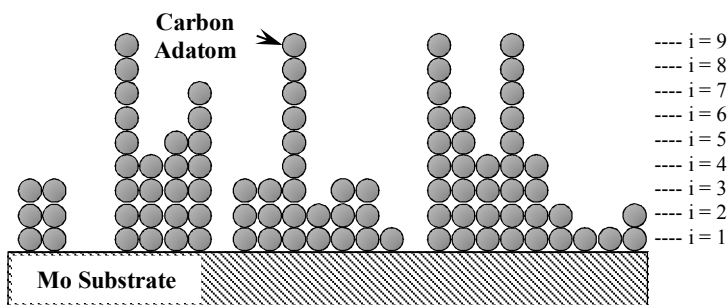


Figure 4.—Illustration of the surface coverage model developed for this study.

The assumptions are appropriate for column-like growth, with the only shortcomings being the lack of the adatom self-shadowing that leads to the columnar structures in the thin film and that the redistribution due to adsorbate layer sputtering was neglected (Ref. 15). If island-type growth is occurring, the impacts of limited surface diffusivity and the redistribution due to adsorbate sputtering are not included in this model. At present, the exact growth mode is unknown.

The surface coverage model developed for this study is illustrated in Figure 4. Because the adsorption of multiple carbon adlayers must be considered, total surface coverage is given by summing the fractional surface coverages of the various adlayers of carbon adatoms, θ_i :

$$\theta_c = \sum_{i=1}^{\infty} \theta_i . \quad (6)$$

And surface area fraction not covered by carbon adatoms, θ_0 , is given by:

$$\theta_0 = 1 - \theta_c . \quad (7)$$

The time rate of change of θ_i is the creation rate of θ_i per unit area minus the removal rate of θ_i per unit area which is given by:

$$N_o \cdot \frac{d\theta_i}{dt} = \text{Creation rate of } \theta_i \text{ per unit area} - \text{Removal rate of } \theta_i \text{ per unit area.}$$

The fractional coverage of adlayer θ_i can be increased by either carbon adsorption onto θ_{i-1} or desorption via sputtering of θ_{i+1} :

$$\gamma_C \cdot s_{i-1} \cdot \theta_{i-1} \equiv \text{Carbon adatom adsorbed onto layer } i-1$$

$$\frac{J_a}{e} \cdot Y_{i+1} \cdot \theta_{i+1} \equiv \text{Carbon adatom desorbed from layer } i+1 .$$

Here, s_i is the adsorbate sticking coefficient on adlayer i and Y_i is the sputter yield of carbon adlayer i . The fractional coverage of adlayer θ_i can be decreased by either carbon adsorption onto θ_i or desorption via sputtering of θ_i :

$$\gamma_C \cdot s_i \cdot \theta_i \equiv \text{Carbon adatom adsorbed onto layer } i$$

$$\frac{J_a}{e} \cdot Y_i \cdot \theta_i \equiv \text{Carbon adatom desorbed from layer } i$$

Substituting the creation and removal rates per unit area above into the time rate of change of θ_i yields for $i \geq 1$:

$$N_o \cdot \frac{d\theta_i}{dt} = \gamma_C \cdot (s_{i-1} \cdot \theta_{i-1} - s_i \cdot \theta_i) + \frac{J_a}{e} \cdot (Y_{i+1} \cdot \theta_{i+1} - Y_i \cdot \theta_i) \quad (8)$$

and for $i = 0$ (i.e., along the molybdenum substrate surface):

$$N_o \cdot \frac{d\theta_0}{dt} = -\gamma_C \cdot s_0 \cdot \theta_0 + \frac{J_a}{e} \cdot Y_1 \cdot \theta_1 . \quad (9)$$

At equilibrium surface coverage, the fractional surface coverage time rate of change is equal to zero, so:

$$\frac{d\theta_c}{dt} = \sum_{i=1}^{\infty} \frac{d\theta_i}{dt} = 0 . \quad (10)$$

After substituting the equations for $d\theta_i/dt$ into the above equation and rearranging, it can be shown that the fractional surface coverage of carbon adsorbate is given by:

$$\theta_c = \frac{\sum_{i=1}^{\infty} \left[\left(\frac{e \cdot \gamma_C}{J_a} \right)^i \cdot \prod_{k=1}^i \frac{S_{k-1}}{Y_k} \right]}{1 + \sum_{i=1}^{\infty} \left[\left(\frac{e \cdot \gamma_C}{J_a} \right)^i \cdot \prod_{k=1}^i \frac{S_{k-1}}{Y_k} \right]} . \quad (11)$$

This equation includes a series summation to infinity, which complicates numerical evaluation. However, this summation to infinity can be eliminated by noting that for $i \geq i_{\max}$ adlayers, carbon adlayer sputter yield and sticking are equivalent to that of bulk carbon and are, therefore, constant (i.e., $Y_i = Y_C$ and $s_i = s_C$, respectively, for $i \geq i_{\max}$). It can, therefore, be shown that the fractional surface coverage of carbon adsorbate is given by:

$$\theta_c = \frac{\left(\prod_{k=1}^{i_{\max}-1} \frac{Y_C \cdot S_{k-1}}{S_C \cdot Y_k} \right) \cdot \left\{ \frac{1}{1 - \frac{e \cdot \gamma_C \cdot S_C}{j_a \cdot Y_C}} - \sum_{i=0}^{i_{\max}-1} \left(\frac{e \cdot \gamma_C \cdot S_C}{j_a \cdot Y_C} \right)^i \right\} + \sum_{i=1}^{i_{\max}-1} \left[\left(\frac{e \cdot \gamma_C}{j_a} \right)^i \cdot \prod_{k=1}^i \frac{S_k - 1}{Y_k} \right]}{1 + \left(\prod_{k=1}^{i_{\max}-1} \frac{Y_C \cdot S_{k-1}}{S_C \cdot Y_k} \right) \cdot \left\{ \frac{1}{1 - \frac{e \cdot \gamma_C \cdot S_C}{j_a \cdot Y_C}} - \sum_{i=0}^{i_{\max}-1} \left(\frac{e \cdot \gamma_C \cdot S_C}{j_a \cdot Y_C} \right)^i \right\} + \sum_{i=1}^{i_{\max}-1} \left[\left(\frac{e \cdot \gamma_C}{j_a} \right)^i \cdot \prod_{k=1}^i \frac{S_{k-1}}{Y_k} \right]} \quad (12)$$

for $j_a > \frac{e \cdot \gamma_C \cdot S_C}{Y_C}$ and:

$$\theta_c = 1 \quad (13)$$

for $j_a \leq \frac{e \cdot \gamma_C \cdot S_C}{Y_C}$. Here, the series summation to infinity was eliminated with the use of a power series expansion.

A value of interest from the above equations is the accelerator current density at the transition from net erosion to net carbon deposition. At this transition, there is complete carbon adsorbate surface coverage, so $\theta_c = 1$. It can be shown that $\theta_c \rightarrow 1$ as:

$$1 - \frac{e \cdot \gamma_C \cdot S_C}{j_a \cdot Y_C} \rightarrow 0. \quad (14)$$

The resulting ion current density is given by:

$$j_{a-trans} = \frac{e \cdot \gamma_C \cdot S_C}{Y_C}. \quad (15)$$

Here, $j_{a-trans}$ is the accelerator ion current density where transition from net erosion to net deposition occurs. This equation shows that the transition is a function of bulk carbon sputter yield and adsorbate sticking coefficient, indicating that the surface is made up of multiple carbon adlayers at complete surface coverage.

The fractional surface coverage from Equation (12) is the more rigorous model used in this study. It accounts for the multiple carbon adlayers prior to complete substrate surface coverage with the aforementioned assumptions. However, this more rigorous model requires knowledge of more terms than that of the original NSTAR analysis. While the NSTAR analysis model required knowledge of γ_C , j_a , and Y_{C-Mo} , this new model also requires knowledge of:

1. adlayer sputter yields Y_i between $Y_1 (= Y_{C-Mo})$ and $Y_{i \geq i_{\max}} (= Y_C)$;
2. carbon adsorbate sticking coefficients s_{Mo} and s_C ;
3. carbon adlayer sticking coefficients s_i between $s_0 (= s_{Mo})$ and $s_{i \geq i_{\max}} (= s_C)$; and
4. i_{\max} for both sputter yield and sticking coefficient.

The next section will define these model inputs.

C. Model Inputs

The following sections will discuss how some carbon surface coverage model inputs were determined. This includes the determination of adsorbate sputter yields, adsorbate sticking coefficients, and accelerator ion current densities in the pit and groove erosion pattern.

1. Adsorbate Sputter Yields

Reference 12 included measurements of sputter yields of a single monolayer of carbon adsorbate on a molybdenum substrate with xenon ions (i.e., $Y_1 = Y_{C-Mo}$). As discussed by Polk et al., there was some concern that their study's measured sputter yields with xenon required a surface binding energy to match their theoretical predictions that was too low (Ref. 12). Since that study, these sputter yields were re-measured by Ho et al. with the results being nearly identical to those of the original study (Refs. 12 and 18). In addition, the Sigmund and Winters theoretical model used in Reference 12 was reviewed by this author and updated with more recent sputter yields, reflection coefficients, and screening potentials for elastic collisions. The resulting theoretical predictions required unrealistically high surface binding energies for favorable comparisons with measurements, indicating that this theoretical model should not be used to draw conclusions about surface binding energy magnitudes. So, for this study, sputter yields of a single monolayer of carbon adsorbate on a molybdenum substrate with xenon ions were those measured by Ho et al. and extrapolated to the lower xenon ion energies of interest in this study (Ref. 18).

The sputter yield of bulk carbon graphite (i.e., Y_C) was used to define the carbon adlayer sputter yields (i.e., Y_i) for $i \geq i_{\max}$. These sputter yields were determined by curve-fitting the carbon sputter yield measurements of Ref. 19 as a function of xenon ion energy.

Thin film sputter yield measurements were used to estimate the number of adlayers required for the carbon adsorbate sputter yield to equal that of bulk carbon (i.e., i_{\max}). Anderson and Bay found that reliable bulk sputter yields could be measured when film thicknesses were $\geq 1/2$ of the projectile range (Ref. 20). The projectile range, R_i , is the total path length of a bombarding ion in a solid material and is given by (Ref. 21):

$$R_i = -\int_{V_{\text{cex}}}^0 \frac{dE}{\left(\frac{dE}{dx}\right)_n + \left(\frac{dE}{dx}\right)_e}. \quad (16)$$

Here, V_{cex} is the ion energy and $(dE/dx)_n$ and $(dE/dx)_e$ are the nuclear (or elastic) and electronic (or inelastic) stopping powers of a xenon projectile in a carbon target. These stopping powers are defined in Reference 21 using a Ziegler, Biersack, and Littmark screening potential. The stopping powers also require a density for the carbon adsorbate. The density of graphite is 2.25 gm/cm^3 , and this density was found to be consistent with the quartz crystal microbalance mass and post-test thickness measurements for the NSTAR LDT (Ref. 12). However, carbon films from the accelerator grid downstream surface were thicker due to enhanced porosity with a corresponding density of 1.35 gm/cm^3 (Ref. 12). This latter carbon density was used to determine adsorbate stopping powers. The number of adlayers required for the carbon adsorbate sputter yield to equal that of bulk carbon, i_{\max} , is given by:

$$i_{\max} = \frac{R_i}{2 \cdot \left(3.35 \times 10^{-10} \text{ m} \cdot \frac{2.25 \times 10^3 \text{ kg/m}^3}{1.35 \times 10^3 \text{ kg/m}^3} \right)}. \quad (17)$$

Here, an average adlayer thickness of half of the lattice parameter perpendicular to hexagonal plane of a graphite lattice (i.e., $3.35 \times 10^{-10} \text{ m}$) was conservatively assumed and this dimension is further modified

with the lower carbon density deposited on the NSTAR grid. For the range of xenon ion energies investigated in this study, the number of adlayers required for the carbon adsorbate sputter yield to equal that of bulk carbon was estimated to be about 3 (i.e., $i_{\max} \approx 3$).

Thin film sputter yield measurements were also used to estimate how sputter yields vary as a function of adlayer number for $1 \leq i \leq i_{\max}$ (i.e., Y_i between Y_{C-Mo} and Y_C). Anderson and Bay measured sputter yield variations of thin gold films on a beryllium substrate as a function of film thickness for thicknesses less than $< \frac{1}{2}$ the projectile range (Ref. 20). Their results showed that the sputter yield varies approximately linearly as a function of adsorbate thickness. Therefore, Y_i was assumed to vary linearly from Y_{C-Mo} to Y_C for $1 \leq i \leq i_{\max}$ for this study.

2. Sticking Coefficient

Sputtered particles are known to be eroded with kinetic energies that follow a Sigmund-Thompson energy distribution function (Ref. 21). For a carbon target eroded by xenon ions, eroded particle energies range from zero to 31 percent of the bombarding ion's kinetic energy with the most probable energy being half of the carbon surface binding energy (i.e., about 3.7 eV) (Refs. 21 and 22). For back-sputtered carbon to be either physisorbed or chemisorbed onto the molybdenum substrate or a carbon adlayer, the back-sputtered carbon's energy normal to surface must first be dissipated via elastic collisions with surface atoms. If the back-sputtered carbon collides with carbon adlayers, the full kinetic energy of the eroded carbon projectile can be elastically transferred in a single collision. However, if back-sputtered carbon collides with the molybdenum substrate, a maximum of only 40 percent of the carbon projectile's kinetic energy can be elastically transferred in a single collision. Because the back-sputtered carbon particle's energy can be large, and in the case of the molybdenum substrate, its energy transfer via collisions is inefficient, back-sputtered carbon reflection can be significant. The fractional number of reflected carbon particles is given by R_N , and therefore, the sticking coefficient is given by $s = 1 - R_N$.

Modeling results from Joh, et al. were used to determine the reflection coefficients for a carbon projectile on molybdenum and carbon targets (Ref. 23). That study yielded reflection coefficients of ~ 0.4 and < 0.07 for a carbon projectile on molybdenum and carbon targets, respectively, for the energy range of interest in this study. But that study assumed that reflected particles with a reflected energy of ≤ 1 eV were adsorbed by the surface (Ref. 23). A more appropriate energy would have been the anticipated chemisorption energy, which would have resulted in a lower reflection coefficient. In an attempt to correct these results for this higher chemisorption energy, the reflection coefficients were integrated over the full Sigmund-Thompson energy distribution range so that projectiles with an energy less than or equal to a conservatively assumed energy of 7.4 eV (i.e., the surface binding energy of carbon) (Ref. 22) were not reflected, but those with a higher energy retained the aforementioned reflection coefficients. The resulting sticking coefficients for a carbon projectile were estimated to be $s_{Mo} \approx 0.7$ for a molybdenum target and $s_C \approx 1.0$ for a carbon target for the full range of energies examined in this study.

Finally, the sticking coefficient at the accelerator grid surface was conservatively assumed to immediately transition from s_{Mo} to s_C with the first adlayer of carbon (i.e., $s_0 = s_{Mo}$ and $s_{i \geq 1} = s_C$ for carbon sticking) for this study.

3. Average Accelerator Current Density

In this study, an average accelerator current density in the pit and groove erosion pattern was estimated using the equation below, which is similar to that used in Reference 12:

$$j_a = j_b \cdot \frac{J_a - J_{av}}{J_b} \cdot \frac{dA_o}{dA_{erode}} \quad (18)$$

Here, j_b is the beam current density along the grid surface, J_a is the accelerator current, J_{aw} is the accelerator current collected at the accelerator aperture walls, J_b is the beam current, and dA_{erode}/dA_o is ratio of the pit and groove eroded area to the hexagon area surrounding single aperture. Note that $J_a - J_{aw}$ represents the total grid current collected at the pit and groove erosion site and that the area surrounding a single aperture is a hexagon because of the hexagonal aperture pattern used for the grids.

For this study, J_a and J_b were averages of the measured values during operation at a particular operating condition. The current J_{aw} was determined using the ion optics code developed in Reference 24. The ratio dA_{erode}/dA_o was determined from pit and groove erosion measurements.

Finally, the beam current density along the grids (i.e., j_b) was rigorously determined using measured downstream beam current densities and an algorithm developed by this author that is similar to that of References 6 and 24. For this algorithm, the ion optics code of Reference 24 is used to develop an empirical equation for the emitted beam current density per steradian as a function of beamlet current along the grid for a given set of grid potentials. Equations were developed for predicting the radial downstream beam current density profile from the spherically-domed grid surface. These equations treat individual beamlets as point sources and assume a direct line-of-sight transmission (i.e., beam ion deflection by downstream potential gradients is neglected). These equations also account for the current emitted by every aperture and for probe area effects, which are important for beam current density measurements close to the thruster grid. The beamlet current distribution along the spherically-domed grid must be integrated to predict the downstream beam current density. However, the downstream beam current density is an algorithm input, so a program was developed to iteratively determine the beamlet current distribution along the grid surface. The beam current density along the grid is just the beamlet current divided by the hexagonal area surrounding an aperture.

A sample output of the aforementioned algorithm is shown in Figure 5 for the NEXT LDT thruster operating at full power. As shown in the figure, the planar probe measurement 2.0 cm downstream of the grids was used to predict the beam current density along the grid surface. Because the NEXT LDT is also equipped with planar probes located 17.3 and 23.8 cm downstream, these can be used to check the algorithm. The results, shown in Figure 6, demonstrate the algorithm’s ability to predict these downstream beam current density profiles.

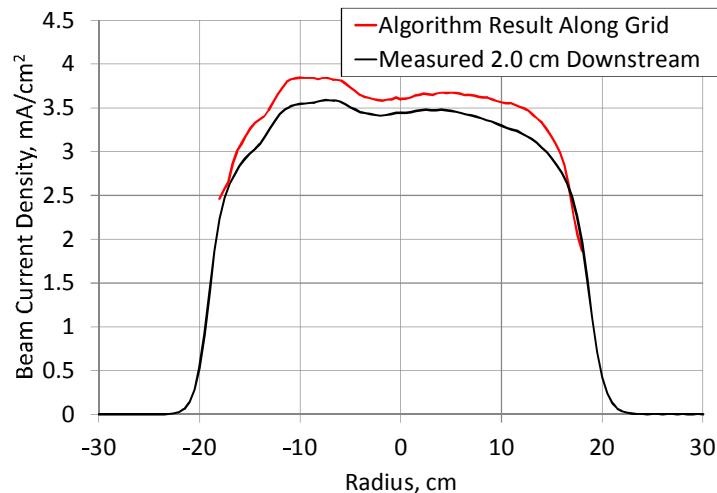


Figure 5.—Measured and predicted beam current densities for the NEXT LDT thruster at full power.

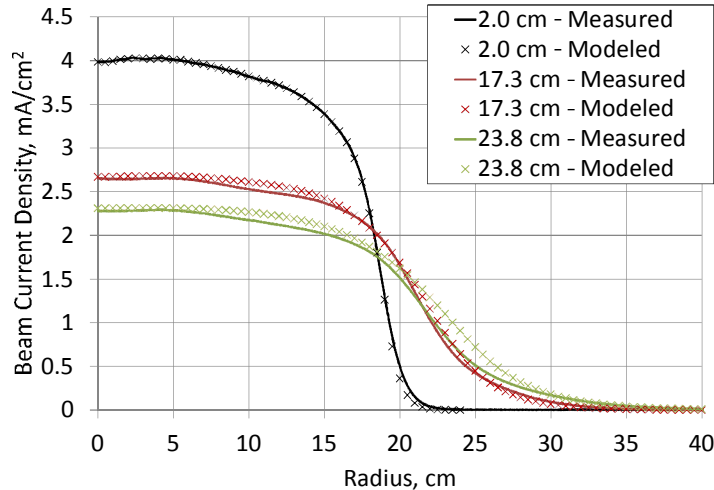


Figure 6.—Measured and predicted beam current densities for the NEXT LDT thruster at full power at various axial locations.

III. Evaluation of Analysis Improvements Using the NSTAR LDT

The objective of this section is to evaluate the improvements made to the analysis and determine sensitivities to the model inputs. This is done by applying the improved analysis approach to the NSTAR LDT. The first section describes test-specific inputs to the analysis. The section thereafter presents and discusses the results of the analysis.

A. NSTAR LDT Analysis Inputs

Test-specific model inputs have to be determined to apply the improved analysis to the NSTAR LDT. During this test, a NSTAR ion thruster was operated at full power throughout the 8,192 h test (Refs. 11 and 12). The NSTAR LDT vacuum facility was internally lined with graphite panels to reduce facility material back-sputtering. The back-sputter rate was measured with a quartz crystal microbalance located next to the thruster and confirmed with post-test film thickness measurements. The back-sputter rate of carbon was determined to be $0.7 \mu\text{m}/\text{kh}$, which corresponded to a carbon flux of 2.19×10^{12} atoms/ $\text{cm}^2 \cdot \text{s}$ (Ref. 12).

The average beam and accelerator currents were 1.76 A and 6.78 mA, respectively (Ref. 12). An ion optics code was used to determine that only 0.96 mA of accelerator current was collected on the accelerator aperture barrels (Ref. 24), which is significantly less than the 3.7 mA estimate in the original NSTAR analysis (Ref. 12). The original NSTAR analysis determined this accelerator current split by using a simple ratio of the measured mass losses from the accelerator grid erosion sites. However, this incorrectly assumes that charge exchange ions that impact aperture barrel walls have the same average energy and sputtering angle of incidence as those of the pit and groove sites. Charge exchange ions that impact the accelerator barrels are created within inter-grid region and have higher average energies and sputter the barrel walls at higher angles of incidence than those of the pit and groove erosion sites (Refs. 25 and 26). Finally, the ratio dA_{erode}/dA_o was inferred from Reference 12 to be 0.312, and this was constant across the accelerator grid.

The beam current density, shown in Figure 7, was measured with a planar probe located 2.5 cm downstream of the grid. Also shown in the figure is the current density along the grid, which was determined by the algorithm of this study. The average accelerator grid current density in the pit and groove erosion pattern from Equation (18) is shown in Figure 8. Note that these current densities are nearly twice those of Reference 12, and this is primarily due to that study's inaccurate accelerator current split. The maximum accelerator current density, $j_{a\text{-max}}$, was $64 \mu\text{A}/\text{cm}^2$ at the center of the grid.

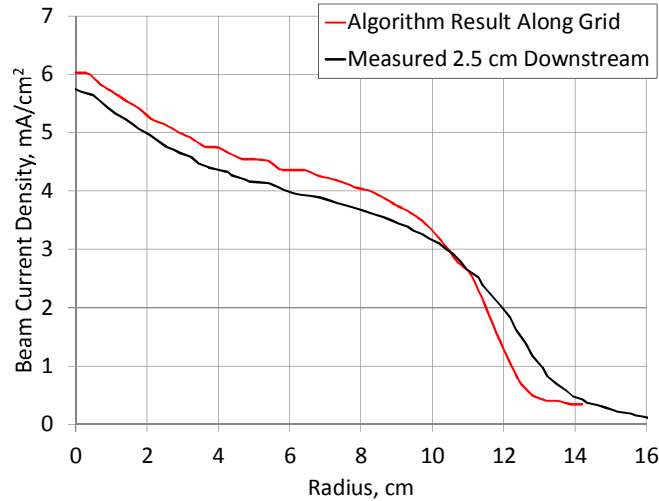


Figure 7.—Measured and predicted beam current densities for the NSTAR LDT thruster at full power.

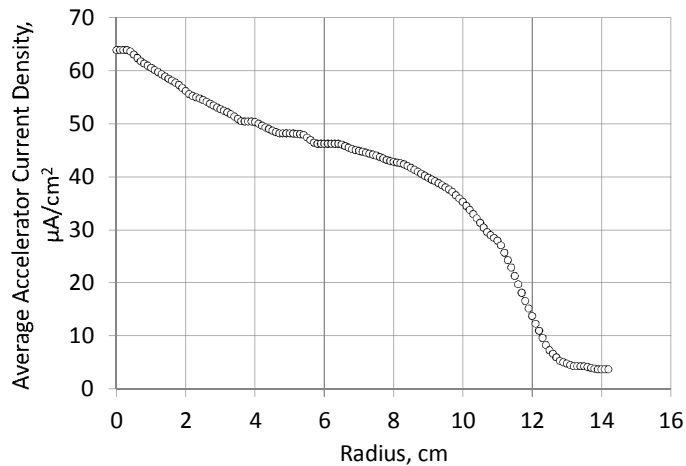


Figure 8.—Estimated average accelerator current density in the pit and groove erosion pattern for the NSTAR LDT thruster at full power.

The maximum accelerator current density is important because its corresponding location on the grid is where failure due to pit and groove erosion would be expected to occur.

The charge exchange ions that erode the pit and groove erosion site are assumed to be created downstream of the accelerator grid sheath, so that they impact this erosion site with a potential, V_{cex} given by:

$$V_{\text{cex}} \approx |V_a| + |V_g| + V_{\text{beam}} \quad (19)$$

Here, V_a is the accelerator power supply voltage (i.e., -180 V for the NSTAR LDT), V_g is the coupling voltage (i.e. -15 V for the NSTAR LDT), and V_{beam} is the beam plasma potential, which is assumed to be 5 V throughout this study. So, charge change ions are assumed to erode the pit and groove erosion site with a 200 V potential for the NSTAR LDT. The resulting sputter yields for a single carbon monolayer on molybdenum (i.e., Y_{C-Mo}) and bulk carbon (i.e., Y_C) were 0.99 and 0.040 , respectively.

The transition from net erosion to net deposition was measured post-test to be at a radial location of 11.8 cm (Ref. 12). This corresponded to a transition accelerator current density of $17 \mu\text{A}/\text{cm}^2$. As will be shown in the next section, this transition current density can be used, in part, to check the analysis.

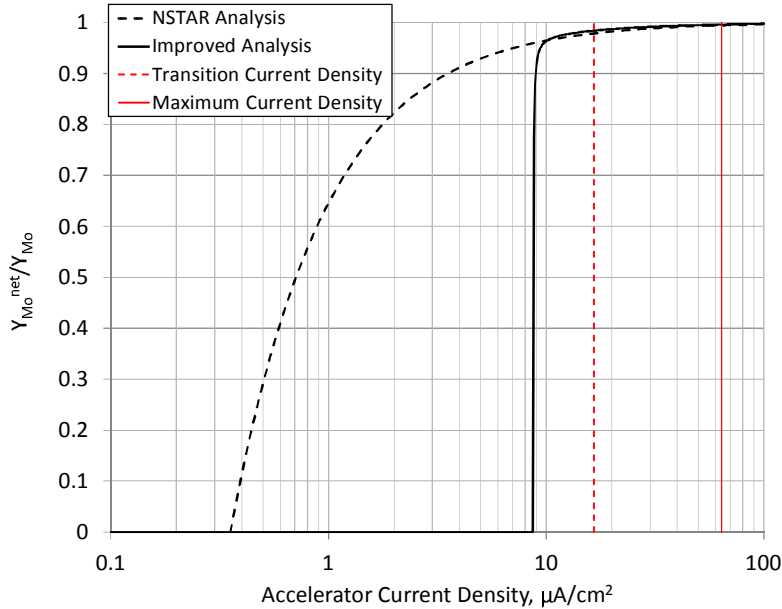


Figure 9.—The ratio of net-to-bulk molybdenum sputter yield as a function of accelerator current density in the pits and grooves for the improved and NSTAR analyses. The input values for the improved analysis were: $Y_{C-Mo} = 0.99$, $Y_C = 0.040$, $i_{max} = 3$, and $s_{Mo} = 0.7$.

B. NSTAR LDT Results and Discussions

Results from the improved analysis are shown in Figure 9 along with NSTAR analysis results for comparison. Note that the only difference between the analyses in this figure is the surface coverage model. The improved analysis utilizes Equations (12) and (13) while the NSTAR analysis utilizes Equation (5). The figure also includes the maximum and transition accelerator current densities determined in the prior section. Figure 9 illustrates that the improved analysis net-to-bulk molybdenum sputtering ratio exhibits a steep drop with decreasing current density near the predicted transition. The NSTAR analysis exhibited a more gradual decrease with decreasing current density. The improved analysis shows that for current densities greater than the transition current density, the impact of back-sputtered carbon on the pit and groove wear rate is insignificant. Or, put differently, the impact of back-sputtered carbon on the pit and groove wear rate is insignificant at the net erosion sites.

Figure 9 also illustrates that the improved analysis predicts the transition current density considerably more accurately than the NSTAR analysis. The measured transition current density is 1.9 times the improved analysis prediction, but is 47 times the NSTAR analysis prediction. Possible causes for the remaining discrepancy between improved analysis' prediction and the measured transition current density include the following:

1. The bombarding ion potential determined by Equation (19) is too high, leading to a high sputter yield. Charge-exchange ions that bombard the pit and groove erosion site have an energy distribution with a maximum of V_{cex} . Though an ion optics code confirmed this (Ref. 24), code results showed that this error only accounts for about a tenth of the discrepancy.
2. The bulk carbon sputter yield used in this study may be incorrect. Bulk carbon sputter yield measurements for xenon at 200 V range from 0.024 to 0.090 (Ref. 27). This study used a yield of 0.040, and this may have been too high (Ref. 19). In addition, the porous surface may be affecting this yield. This porous surface could have led to increased re-deposition, leading to an overall reduction in sputter yield (Ref. 20).

3. A poor assumption or error in the determination of the transition accelerator current density may be contributing to the discrepancy. For example, Figure 8 shows that the radial location for this transition (i.e., 11.8 cm) occurs where the accelerator current density was changing significantly as a function of radius. This could have introduced error in the measured transition accelerator current density.
4. A poor assumption used for the carbon surface coverage model may be contributing to the discrepancy. For example, the surface coverage model is a simple one-dimensional model. However, there may be two- and three-dimensional effects, such as buildup of carbon deposition surrounding the pits and grooves, that are leading to a local increase in carbon flux to the erosion site. This would lead to a higher transition current density.

Figure 10 illustrates the sensitivity of the new carbon surface coverage model of Equations (12) and (13) to the model inputs Y_1 , i_{\max} , and s_0 . Figure 10 shows that increasing Y_1 from an unrealistically low value of Y_C (i.e., 0.040) to Y_{C-Mo} (i.e., 0.99) and i_{\max} from 2 to 3 causes the ratio of net-to-bulk molybdenum to exhibit a significantly steeper drop with decreasing current density. Decreasing s_0 from 1 to s_{Mo} (i.e., 0.7) had a similar effect, but it was not as pronounced as that from the other inputs. This is an indication that the first carbon adlayer (i.e., θ_1) is dictating the shape of the curve. This is further demonstrated in Figure 11 for the fractional surface coverages of the various adlayers as a function of accelerator current density. The first adlayer dominates the total carbon surface coverage for much of the current density range. It is only near the transition current density that the surface coverages of the subsequent adlayers impact the shape of the total surface coverage profile. Figure 11 shows that at the transition current density, the surface coverage of the adlayers displayed decrease abruptly because of rapid adlayer buildup due to decreased desorption via sputtering.

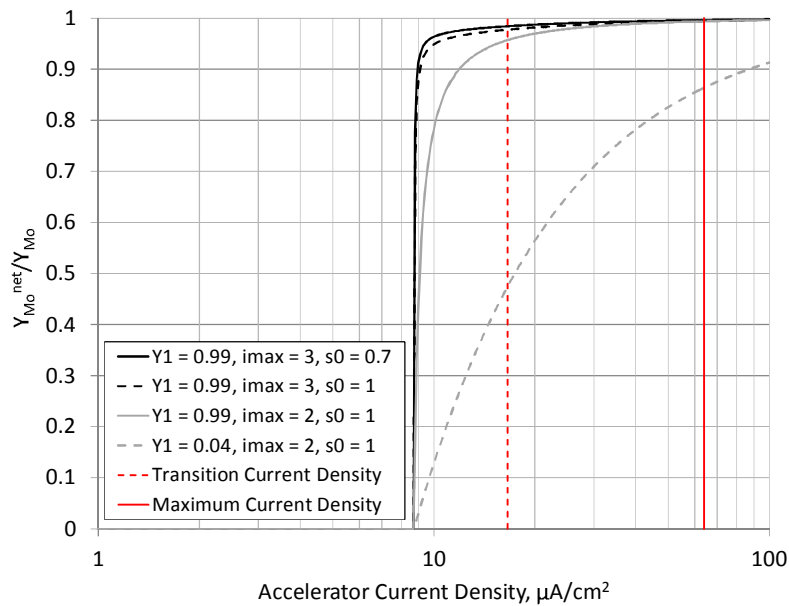


Figure 10.—The ratio of net-to-bulk molybdenum sputter yield as a function of accelerator current density in the pits and grooves for various values of Y_1 , i_{\max} , and s_0 .

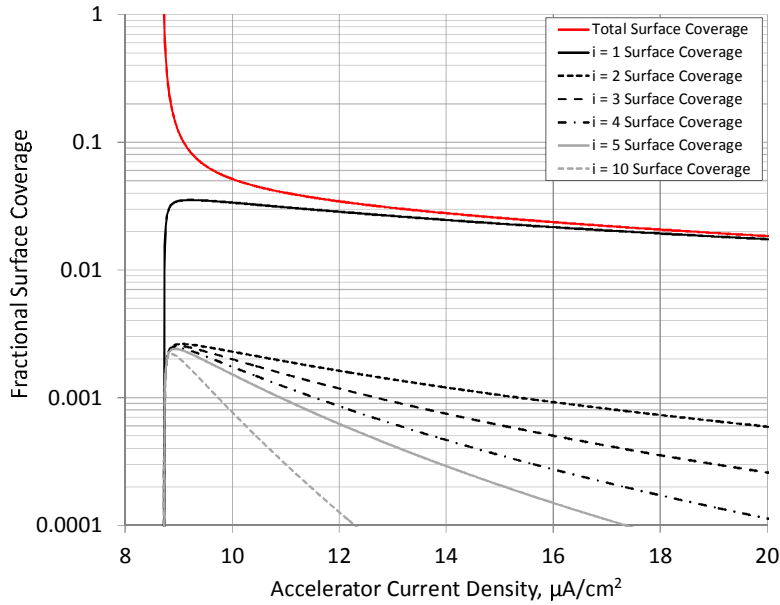


Figure 11.—The fractional surface coverage of various adlayers (i.e., θ_i) and the total carbon surface coverage (i.e., θ_c) as a function of accelerator current density in the pits and grooves. The input values were: $Y_{C-Mo} = 0.99$, $Y_C = 0.040$, $i_{max} = 3$, and $s_{Mo} = 0.7$.

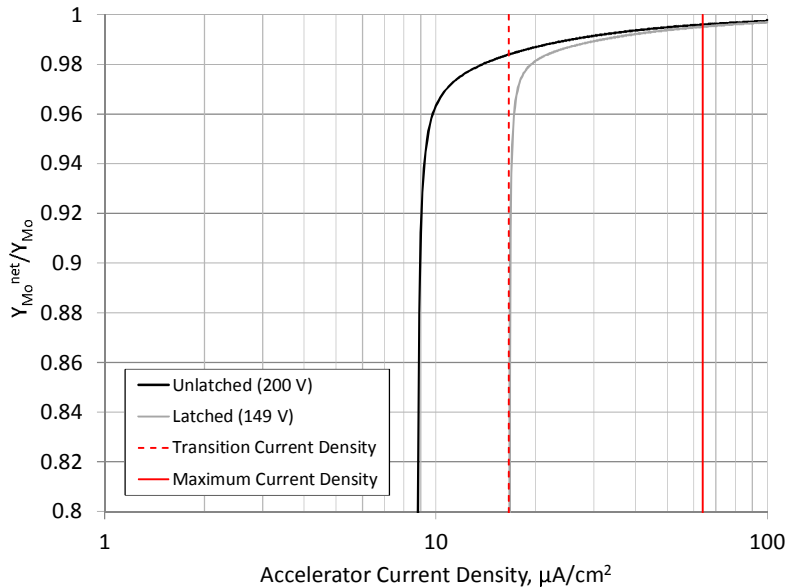


Figure 12.—The NSTAR LDT ratio of net-to-bulk molybdenum sputter yield as a function of accelerator current density in the pits and grooves using the improved analysis for latched and unlatched ion energies.

Figure 12 shows the ratio of net-to-bulk molybdenum sputtering from Figure 9 at the transition current density more clearly. The figure shows two solutions. The “unlatched” solution uses Equation (19) to determine V_{cex} (i.e., 200 V). The “latched” solution uses the measured transition current density to determine V_{cex} (i.e., 149 V) and represents a conservative estimate because the reduced ion energy decreases Y_{C-Mo} , which may not be occurring here. For either solution, however, Figure 12 shows that the impact of back-sputtered carbon on pit and groove erosion for the NSTAR LDT was negligible throughout most of eroded grid radius.

IV. Application of the Improved Analysis to the NEXT LDT

The improved analysis was used to estimate the impact of back-sputtered carbon on the accelerator grid pit and groove wear rate of the NEXT LDT. The first section describes test-specific inputs to the analysis. The section thereafter presents and discusses the results of the analysis.

Unlike the NSTAR analysis, the NEXT LDT analysis is more challenging because the thruster was operated for extended durations at various operating conditions as shown in Table 1. In addition, the test is ongoing, so direct measurements of back-sputtered carbon film thicknesses and grid wear cannot be made. As a result, the NEXT LDT estimates presented herein are considered preliminary until the results of future post-test measurements are incorporated. The following analyses will estimate the impact of back-sputtered carbon on the accelerator grid wear for all extended operating conditions during the NEXT LDT.

A. NEXT LDT Analysis Inputs

The NEXT LDT vacuum facility was internally lined with graphite panels to reduce facility material back-sputtering, and the back-sputter rate was measured with a quartz crystal microbalance located next to the thruster (Refs. 28 and 29). Although the quartz crystal microbalance failed during the first full power test segment, measurements made during regularly scheduled performance tests were used to determine the back-sputter rates for the operating conditions of Table 1. The resulting estimated carbon back-sputter rates are shown in Table 2.

TABLE 1.—THRUSTER OPERATING CONDITIONS, DURATIONS, AND PROPELLANT THROUGHPUT DURING THE NEXT LDT IN CHRONOLOGICAL ORDER

Operating condition ^a	Segment duration, h	Post-segment duration, h	Segment throughput, ^b kg	Post-segment throughput, ^b kg
3.52 A, 1800 V	13,042	13,042	264.7	264.7
3.52 A, 1179 V	6,478	19,520	132.6	397.3
1.20 A, 679 V	3,411	22,931	26.7	424.0
1.00 A, 275 V	3,198	26,129	23.4	447.4
1.20 A, 1800 V	3,111	29,240	24.5	471.9
3.52 A, 1800 V	^c 20,265	^c 49,505	^c 415.9	^c 887.8

^aBeam current and beam power supply voltage.

^bXenon propellant.

^cAs of August 8, 2013.

TABLE 2.—NEXT LDT BACK-SPUTTER RATES, AVERAGE MEASURED ACCELERATOR CURRENTS, MODELED APERTURE WALL CURRENTS, AND ERODED AREA RATIOS FOR ALL OPERATING CONDITIONS

Operating condition ^a	Back-sputter rate, $\mu\text{m}/\text{kh}$ ^b	Average accelerator current (J_a), mA	Accelerator barrel current (J_{aw}), ^c mA	Eroded area ratio (dA_{erode}/dA_o) ^d
3.52 A, 1800 V	3.00	14.0	0.92	0.278
3.52 A, 1179 V	1.70	14.4	3.51	0.233
1.20 A, 679 V	0.35	2.35	0.30	0.205
1.00 A, 275 V	0.38	2.21	0.50	0.223
1.20 A, 1800 V	1.28	2.47	0.07	0.174
3.52 A, 1800 V	3.00	13.4	0.92	0.278

^aBeam current and beam power supply voltage.

^bAssumes a carbon density of $2.25 \text{ gm}/\text{cm}^3$.

^cUsing the ion optics code of Reference 24.

^dAssumed constant throughout the grid.

Also shown in Table 2 are the average measured accelerator currents and the modeled current collected at the aperture barrel walls at each operating condition. The eroded area ratio, dA_{erode}/dA_o , was determined with images of the center accelerator aperture, a sample of which is shown in Figure 1. Net erosion site areas were measured from the images taken at the end of each test segment. This eroded area was assumed to be constant throughout the grid. The resulting eroded area ratios are also listed in Table 2.

For the NEXT LDT, beam current densities were measured, in part, with a planar probe located 2.0 cm downstream of the accelerator grid. An example of a beam current density profile at full power is shown in Figure 5. These measurements were used to determine the beam current density along the grid using the algorithm discussed earlier. The resulting profiles were then used with the results of Table 2 to determine the average accelerator current density in the pits and grooves along the grid using Equation (18). The resulting accelerator current density profiles are shown in Figure 13 for the different operating conditions. The slight difference for the two full power profiles is due to the accelerator current difference in Table 2. Figure 13 shows that the maximum accelerator current density was off-center and typically located at a radial location of about -7 cm. The maximum accelerator current density for each operating condition is listed in Table 3.

The transition from net erosion to net deposition for each operating condition was determined from far-field thruster images taken with a high magnification zoom lens. A sample image taken at the end of the first full power test segment is shown in Figure 14. The resolution of these images was sufficient to discern individual apertures and their surrounding erosion pattern. The radial location for transition from net erosion to net deposition was determined from images taken at the end of each operating condition, and the corresponding transition accelerator current density determined with the results of Figure 13. The transition radial location and current density for each operating condition are listed in Table 3.

The charge exchange ion energy, V_{cex} , was determined using two methods. For the first method, the energy was determined with Equation (19) using accelerator voltage settings and average coupling voltages measured during each operating condition. The resulting values using this energy are termed “unlatched.” For the second method, the measured transition current densities listed in Table 3 were used to determine V_{cex} using Equation (15). The resulting values from this method are termed “latched” and represent a conservative result. The unlatched and latched ion energies and the resulting sputter yields are listed in Table 4 for all operating conditions.

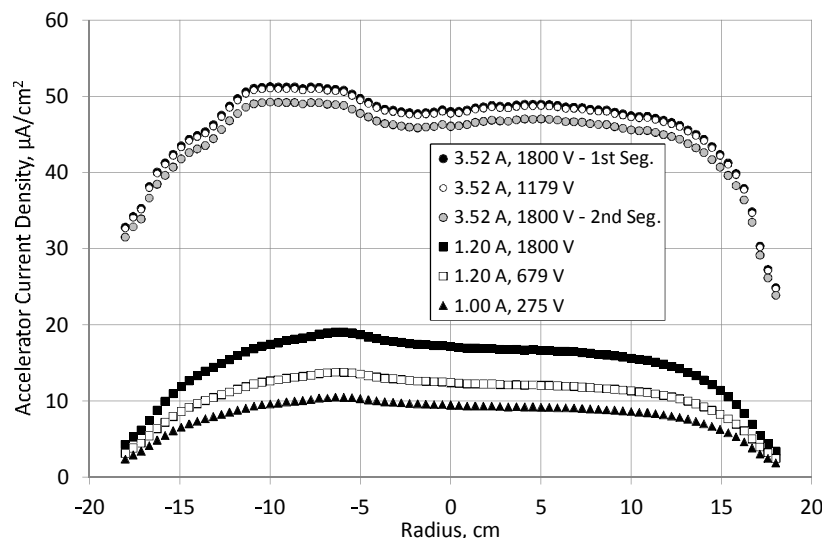


Figure 13.—Average accelerator current density in the pits and grooves as a function of radius for all NEXT LDT operating conditions.

TABLE 3.—NEXT LDT NET EROSION TO NET DEPOSITION TRANSITION RADIAL LOCATIONS AND ACCELERATOR CURRENT DENSITIES, AND MAXIMUM ACCELERATOR CURRENT DENSITIES FOR ALL OPERATING CONDITIONS

Operating condition ^a	Transition radius, cm ^b	Transition accelerator current density ($j_{a-trans}$), $\mu\text{A}/\text{cm}^2$	Maximum accelerator current density (j_{a-max}), $\mu\text{A}/\text{cm}^2$
3.52 A, 1800 V	10.4	47.4	51.2
3.52 A, 1179 V	11.1	47.0	51.0
1.20 A, 679 V	9.5	12.1	13.8
1.00 A, 275 V	11.1	8.88	10.5
1.20 A, 1800 V	6.8	16.5	19.0
3.52 A, 1800 V	11.9	44.9	49.2

^aBeam current and beam power supply voltage.

^bPositive radial locations only.

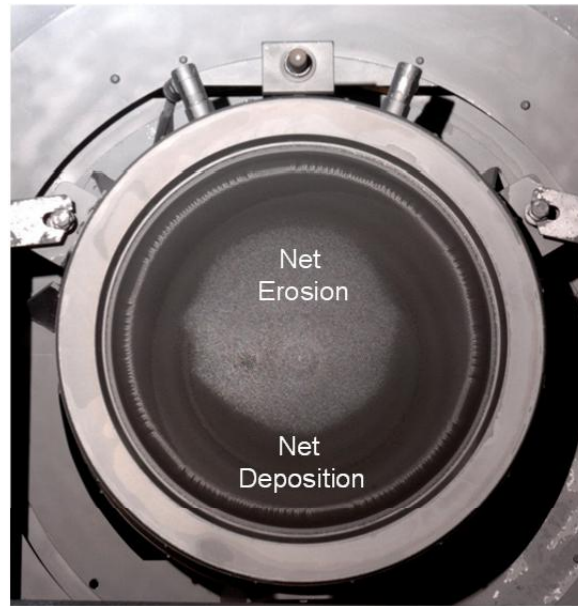


Figure 14.—NEXT LDT far-field image showing the net erosion and net deposition areas along the accelerator grid. The image was taken at 13,042 h following the first full power test segment.

TABLE 4.—NEXT LDT UNLATCHED AND LATCHED ION ENERGIES AND THE RESULTING SPUTTER YIELDS FOR ALL OPERATING CONDITIONS

Operating condition ^a	Unlatched values			Latched values		
	Ion energy, eV	Y_{C-Mo} ^b	Y_C ^c	Ion energy, eV	Y_{C-Mo} ^b	Y_C ^c
3.52 A, 1800 V	225	1.09	0.050	177	0.91	0.032
3.52 A, 1179 V	215	1.05	0.046	141	0.79	0.018
1.20 A, 679 V	129	0.75	0.014	131	0.76	0.015
1.00 A, 275 V	364	1.88	0.11	142	0.79	0.019
1.20 A, 1800 V	225	1.09	0.050	196	0.98	0.039
3.52 A, 1800 V	226	1.10	0.050	182	0.93	0.034

^aBeam current and beam power supply voltage.

^bExtrapolated sputter yields from Reference 18.

^cInterpolated and extrapolated sputter yields from Reference 19.

B. NEXT LDT Results and Discussions

A sample result is plotted in Figure 15 for the first full power test segment. As with the NSTAR LDT results, the improved analysis under-predicts the transition accelerator current density, so a latched, conservative solution is shown as well. A comparison of Figures 15 and 12 shows that the net eroded accelerator current density range (i.e., the current densities between transition and maximum) is smaller for the NEXT LDT at full power than that for the NSTAR LDT. This occurred for two reasons. First, the carbon back-sputter rate was much higher in NEXT LDT than that for the NSTAR test. At full power, the NEXT back-sputter rate was over four times that of the NSTAR test, and this was due to the higher beam currents and voltages of the NEXT thruster. Second, the NEXT thruster has a much flatter beam current density profile. As a direct result, the accelerator current density across the grid does not vary as much for the NEXT thruster (Fig. 13) as it does for the NSTAR thruster (Fig. 8). Regardless, Figure 15 does illustrate that the impact of carbon back-sputtering for the NEXT LDT is not significant at the maximum accelerator current density, which is where first failure would be expected to occur.

Table 5 compares the predicted transition accelerator current densities using unlatched ion energies with those determined from measurements in Table 3. The table shows that the disparities were less than the 47 percent disparity of the NSTAR LDT comparison except for two cases. But these two larger disparities had two common attributes. First, operation during that operating condition required the removal of net carbon deposition. Second, the predicted transition accelerator current density was so low that net carbon deposition had to be removed from the entire perforated grid. The duration at these operating conditions was likely insufficient to remove so much net carbon deposition, and this led to the larger disparities.

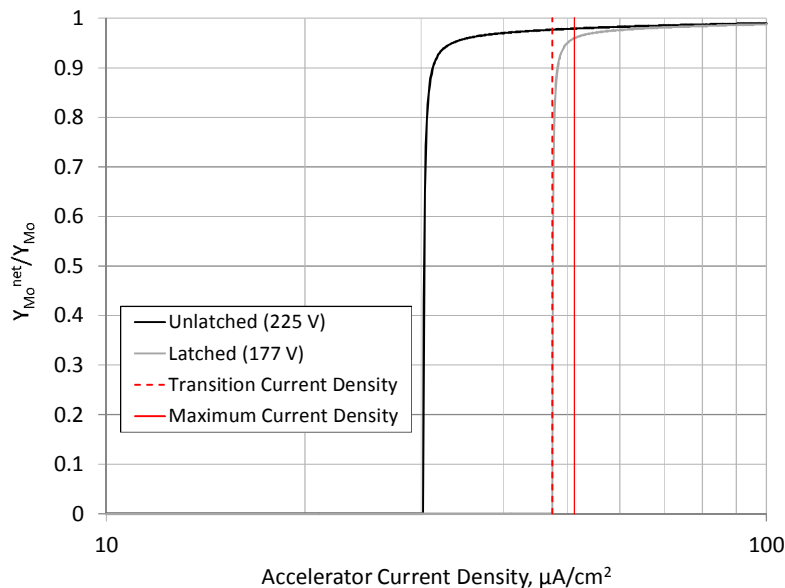


Figure 15.—The NEXT LDT ratio of net-to-bulk molybdenum sputter yield as a function of accelerator current density in the pits and grooves for unlatched and latched ion energies. Results shown are for the first full power operating condition.

TABLE 5.—NEXT LDT PREDICTED AND MEASURED TRANSITION ACCELERATOR CURRENT DENSITIES FOR ALL OPERATING CONDITIONS

Operating condition ^a	Transition radius, cm	Transition accelerator current density ($j_{a-trans}$), $\mu\text{A}/\text{cm}^2$		Disparity, percent
		Predicted	Measured	
3.52 A, 1800 V	10.4	30.2	47.4	36
3.52 A, 1179 V	11.1	^b 18.6	47.0	^c 60
1.20 A, 679 V	9.5	12.7	12.1	-5.2
1.00 A, 275 V	11.1	^b 1.6	8.88	^c 82
1.20 A, 1800 V	6.8	12.9	16.5	21
3.52 A, 1800 V	11.9	30.1	44.9	33

^aBeam current and beam power supply voltage.

^bPositive radial locations only.

^cPredicted transition current density requires removal of net carbon deposition from entire perforated grid.

TABLE 6.—NEXT LDT UNLATCHED AND LATCHED NET-TO-BULK MOLYBDENUM SPUTTER YIELD FOR ALL OPERATING CONDITIONS

Operating condition ^a	Y_{Mo}^{net}/Y_{Mo} at j_{a-max}	
	Unlatched V_{ces}	Latched V_{ces}
3.52 A, 1800 V	0.979	0.960
3.52 A, 1179 V	0.988	0.978
1.20 A, 679 V	0.984	^b 0.985
1.00 A, 275 V	0.994	0.983
1.20 A, 1800 V	0.975	0.965
3.52 A, 1800 V	0.978	0.961

^aBeam current and beam power supply voltage.

^bThe latched ion energy was higher than the unlatched energy, so the latched result is more conservative for this operating condition.

The impact of back-sputtered carbon on the pit and groove erosion rate of the downstream accelerator grid is listed in Table 6 for all operating conditions. Shown in the table are the unlatched and the more conservative latched results. The results are evaluated at the maximum accelerator current densities because this is where first failure would be expected to occur. The table shows that the worst-case impact of carbon back-sputtering was the full power operating condition. However, the maximum impact of back-sputtered carbon was only a four percent reduction in pit and groove erosion rate. As a result, back-sputtered carbon is estimated to have an insignificant impact on the first failure mode of the NEXT LDT at all operating conditions. The results of this analysis will be updated with the results of future post-test measurements.

Conclusions

Accelerator grid wear rates are affected by two competing facility-induced effects: facility background pressures that enhance grid wear rates and facility back-sputtered material that reduces grid wear rates. A study was conducted to quantify the impact of back-sputtered carbon on the downstream accelerator grid erosion rates of the NEXT LDT. A similar analysis that was conducted for the NSTAR LDT was used as a foundation for the improved analysis developed herein. The general model for the impact of back-sputtered carbon on accelerator grid wear rate was the same as that developed for the NSTAR LDT, where it was conservatively assumed that any carbon surface coverage eliminates molybdenum substrate sputtering. An investigation of the likely adsorbate growth modes revealed there are multiple carbon adlayers before complete surface coverage is achieved. As a result, any carbon surface coverage model must account for these multiple carbon adlayers. A more rigorous carbon surface coverage model was developed using a model that was originally used to describe the physisorption of additional gas adlayers on a chemisorbed adlayer. The resulting model requires knowledge of more model inputs, so they were conservatively estimated using the results of past thin film sputtering studies and

particle reflection predictions. In addition, accelerator current densities along the grid were rigorously determined using an ion optics code to determine accelerator current distributions and an algorithm that was developed to determine beam current densities along the grid using downstream density measurements.

The improved analysis was applied to the NSTAR LDT results for evaluation. Model inputs were rigorously defined. Afterwards, the improved analysis was applied to the NSTAR test. The net-to-bulk molybdenum sputtering ratio of the improved analysis exhibited a steep drop with decreasing current density near the predicted transition accelerator current density. The original NSTAR analysis exhibited a more gradual decrease with decreasing current density. The new analysis shows that the impact of back-sputtered carbon on the pit and groove wear rate is insignificant at the net erosion sites throughout most of the grid. The improved analysis was found to predict the transition current density considerably more accurately than the original NSTAR analysis. Causes for the remaining discrepancy included incorrect bombarding ion energies or bulk carbon sputter yields, accelerator current density determination errors, and a potentially poor surface coverage model assumption. To conservatively account for the transition current density discrepancy, a “latched” solution was developed that used the measured transition current density to determine bombarding ion energy. Results showed that the impact of back-sputtered carbon on pit and groove wear rate of the NSTAR LDT was negligible throughout most of eroded grid radius.

The improved analysis was then used to estimate the impact of back-sputtered carbon on the accelerator grid pit and groove wear rate of the NEXT LDT. Unlike the NSTAR analysis, the NEXT LDT analysis was more challenging because the thruster was operated for extended durations at various operating conditions, and the thruster was unavailable for measurements because the test is ongoing. As a result, the NEXT LDT estimates presented herein are considered preliminary. Model inputs were defined for every operating condition, and the improved analysis was then applied to each condition. NEXT LDT back-sputter rates were higher and accelerator current density variations across the grid were smaller, so the net eroded accelerator current density range was smaller than that for the NSTAR LDT. Disparities between predicted and measured accelerator transition current densities were typically less than the 47 percent disparity of the NSTAR LDT comparison. The impact of back-sputtered carbon on pit and groove wear rate was evaluated at the maximum accelerator current densities because this is where first failure would be expected to occur. The maximum impact of back-sputtered carbon was only a four percent reduction in pit and groove erosion rate. As a result, back-sputtered carbon is estimated to have an insignificant impact on the first failure mode of the NEXT LDT at all operating conditions. These preliminary estimates will be updated with the results of future post-test measurements.

References

1. Patterson, M.J. and Benson, S.W., “NEXT Ion Propulsion System Development Status and Performance,” *43rd AIAA/ASME/SAE/ASEE Joint Propulsion Conference and Exhibit*, AIAA Paper 2007-5199, Cincinnati, Ohio, July 2007.
2. Polk, J.E., et al., “Demonstration of the NSTAR Ion Propulsion System on the Deep Space One Mission,” *27th International Electric Propulsion Conference*, IEPC Paper 2001-075, Pasadena, California, October 2001.
3. Garner, C.E., et al., “In-Flight Operation of the Dawn Ion Propulsion System Through Orbit Capture at Vesta,” *47th AIAA/ASME/SAE/ASEE Joint Propulsion Conference & Exhibit*, AIAA Paper 2011-5661, San Diego, California, July-August 2011.
4. Benson, S.W. and Patterson, M.J., “NEXT Ion Propulsion System Progress Towards Technology Readiness,” *44th AIAA/ASME/SAE/ASEE Joint Propulsion Conference & Exhibit*, AIAA Paper 2008-5285, Hartford, Connecticut, July 2008.
5. Van Noord, J.L. and Herman, D.A., “Application of the NEXT Ion Thruster Lifetime Assessment to Thruster Throttling,” *44th AIAA/ASME/SAE/ASEE Joint Propulsion Conference & Exhibit*, AIAA Paper 2008-4526, Hartford, Connecticut, July 2008.

6. Brophy, J.R., "Propellant Throughput Capability of the Dawn Ion Thrusters," *30th International Electric Propulsion Conference*, IEPC Paper 2007-279, Florence, Italy, September 2007.
7. Shastry, R., et al., "NASA's Evolutionary Xenon Thruster (NEXT) Long-Duration Test as of 736 kg of Propellant Throughput," *48th AIAA/ASME/SAE/ASEE Joint Propulsion Conference & Exhibit*, AIAA Paper 2012-4023, Atlanta Georgia, July-August 2012.
8. Van Noord, J.L., Soulas, G.C., and Sovey, J.S., "NEXT PM1R Ion Thruster and Propellant Management System Wear Test Results," *31st International Electric Propulsion Conference*, IEPC Paper 2009-163, Ann Arbor, Michigan, September 2009.
9. Soulas, G.C., et al., "NEXT Ion Engine 2000 Hour Wear Test Results," *40th AIAA/ASME/SAE/ASEE Joint Propulsion Conference and Exhibit*, AIAA Paper 2004-3791, Fort Lauderdale, Florida, July 2004.
10. Sengupta, A., et al., "An Overview of the Results from the 30,000 hr Life Test of Deep Space 1 Flight Spare Ion Engine," *40th AIAA/ASME/SAE/ASEE Joint Propulsion Conference and Exhibit*, AIAA Paper 2004-3608, Fort Lauderdale, Florida, July 2004.
11. Polk, J.E., et al., "The Results of an 8200 Hour Wear Test of the NSTAR Ion Thruster," *35th AIAA/ASME/SAE/ASEE Joint Propulsion Conference and Exhibit*, AIAA Paper 1999-2446, Los Angeles, California, June 1999.
12. Polk, J.E., et al., "The Effect of Carbon Deposition on Accelerator Grid Wear Rates in Ion Engine Ground Testing," *36th AIAA/ASME/SAE/ASEE Joint Propulsion Conference and Exhibit*, AIAA Paper 2000-3662, Huntsville, Alabama, July 2000.
13. Winters, H.F. and Sigmund, P., "Sputtering of Chemisorbed Gas (Nitrogen on Tungsten) by Low Energy Ions," *Journal of Applied Physics*, vol. 45, no. 11, November 1974, pp. 4760-4766.
14. Wasa, K. and Hayakawa, S., *Handbook of Sputter Deposition Technology: Principles, Technology, and Applications*, Noyes Publication, Park Ridge, New Jersey, 1992, pp. 10-11.
15. Greene, J.E., "Nucleation, Film Growth, and Microstructural Evolution," *Handbook of Deposition Technologies for Films and Coatings: Science, Technology and Applications*, 2nd Edition, edited by Bunshah, R.F., Noyes Publication, Park Ridge, New Jersey, 1994, pp. 681-739.
16. Brunauer, S., Emmett, P.H., and Teller, E., "Adsorption of Gases in Multimolecular Layers," *Journal of the American Chemical Society*, vol. 60, February 1938, pp. 309-319.
17. Van Noord, J.N., "NEXT Ion Thruster Thermal Model," *43rd AIAA/ASME/SAE/ASEE Joint Propulsion Conference and Exhibit*, AIAA Paper 2007-5218, Cincinnati, Ohio, July 2007.
18. Ho, C., et al. "Desorption of Chemisorbed Carbon on Mo (1 0 0) by Noble Gas Ion Sputtering: Validation of Ground Test Measurements of Ion Engine Lifetimes," *Applied Surface Science*, vol. 252, 2006, pp. 2657-2664.
19. Rosenberg, D. and Wehner, G.K., "Sputtering Yields for Low Energy He⁺, Kr⁺, and Xe⁺-Ion Bombardment," *Journal of Applied Physics*, vol. 33, May 1962, pp. 1842-1845.
20. Andersen, H.H. and Bay, H.L., "Sputter Yield Measurements," *Sputtering by Particle Bombardment I*, edited by Behrisch, R., Springer Verlag, Berlin, 1981, pp. 153-163.
21. Betz, G. and Wien, K., "Energy and Angular Distributions of Sputtered Particles," *International Journal of Mass Spectroscopy and Ion Processes*, vol. 140, 1994, pp. 1-110.
22. Yamamura, Y. and Tawara, H., "Energy Dependence of Ion-Induced Sputtering Yields From Monatomic Solids at Normal Incidence," *Atomic Data and Nuclear Data Tables*, vol. 62, 1996, pp. 149-253.
23. Joh, D. et al., "Energy Distribution of Low-Energy Plasma Ions Reflected from Metal Surfaces by Using a Monte Carlo Calculation," *Journal of the Korean Physical Society*, vol. 37, no. 3, September 2000, pp. 232-235.
24. Farnell, C.C., "Performance and Lifetime Simulation of Ion thruster Optics," Ph.D. Dissertation, Department of Mechanical Engineering, Colorado State University, Fort Collins, Colorado, 2007.
25. Brophy, J.R., et al., "Numerical Simulations of Ion Thruster Accelerator Grid Erosion," *38th AIAA/ASME/SAE/ASEE Joint Propulsion Conference & Exhibit*, AIAA Paper 2002-4261, Indianapolis, Indiana, July 2002.

26. Wang, J., et al., “Three-Dimensional Particle Simulations of NSTAR Ion Optics,” *27th International Electric Propulsion Conference*, IEPC Paper 2001-085, Pasadena, California, October 2001.
27. Kolasinski, R.D., et al., “Carbon Sputtering Yield Measurements at Grazing Incidence,” *42nd AIAA/ASME/SAE/ASEE Joint Propulsion Conference & Exhibit*, AIAA Paper 2006-4337, Sacramento, California, July 2006.
28. Herman, D.A., Soulas, G.C., and Patterson, M.J., “NEXT Long-Duration Test Plume and Wear Characteristics After 16,550 h of Operation and 337 kg of Xenon Processed,” *44th AIAA/ASME/SAE/ASEE Joint Propulsion Conference and Exhibit*, AIAA Paper 2008-4919, Hartford, Connecticut, July 2008.
29. Herman, D.A., Soulas, G.C., and Patterson, M.J., “Status of the NEXT Long-Duration Test After 23,300 Hours of Operation,” *45th AIAA/ASME/SAE/ASEE Joint Propulsion Conference & Exhibit*, AIAA Paper 2009-4917, Denver, Colorado, August 2009.

